Spatial and temporal organization of cadherin in punctate adherens junctions

Indrajyoti Indra[a], Jongho Choi[a], Chi-Shuo Chen[a,1], Regina B. Troyanovsky[a], Lawrence Shapiro[b,c,2], Barry Honig[b,c,d,e,f,2], and Sergey M. Troyanovsky[a,2]

[a]Department of Dermatology, The Feinberg School of Medicine, Northwestern University, Chicago, IL 60611; [b]Department of Biochemistry and Molecular Biophysics, Columbia University, New York, NY 10032; [c]Zuckerman Mind Brain Behavior Institute, Columbia University, New York, NY 10027; [d]Center for Computational Biology and Bioinformatics, Columbia University, New York, NY 10032; [e]Department of Systems Biology, Columbia University, New York, NY 10032; and [f]Howard Hughes Medical Institute, Columbia University, New York, NY 10032

Contributed by Barry Honig, March 5, 2018 (sent for review November 30, 2017; reviewed by Barry M. Gumbiner and Alpha Yap)

Adherens junctions (AJs) play a fundamental role in tissue integrity; however, the organization and dynamics of the key AJ transmembrane protein, E-cadherin, both inside and outside of AJs, remain controversial. Here we have studied the distribution and motility of E-cadherin in punctate AJs (pAJs) of A431 cells. Using single-molecule localization microscopy, we show that pAJs in these cells reach more than 1 μm in length and consist of several cadherin clusters with crystal-like density interspersed within sparser cadherin regions. Notably, extrajunctional cadherin appears to be monomeric, and its density is almost four orders of magnitude less than observed in the pAJ regions. Two alternative strategies of tracking cadherin motion within individual junctions show that pAJs undergo actin-dependent rapid—on the order of seconds—internal reorganizations, during which dense clusters disassemble and their cadherins are immediately reused for new clusters. Our results thus modify the classical view of AJs by depicting them as mosaics of cadherin clusters, the short lifetimes of which enable stable overall morphology combined with rapid internal rearrangements.

cadherin | actin | adhesion | adherens junction

Adherens junctions (AJs) serve as major intercellular adhesive structures in nearly all vertebrates (1, 2). While AJs are extremely diverse in their morphology, they all employ classical cadherin that forms intercellular adhesive bonds, the distribution, strength, and dynamics of which are controlled in part by catenins, cytosolic cadherin-bound proteins (3–6). Despite being a key component of cell–cell adhesion, many basic issues, such as the detailed structure of AJs, mechanisms of their plasticity, and homeostasis, remain to be clarified.

Traditional light and electron microscopy (EM) have identified two major groups of AJs: linear AJs (lAJ) or *zonula adherens* and punctate AJs (pAJ) or *puncta adhaerentia* (7, 8), each of which can be further classified into a variety of subtypes. The lAJs connect polarized epithelial cells along the apex of their lateral membranes. They are relatively immobile, associate with the prominent circumferential actomyosin ring, and may extend up to 1–2 μm along the *z* axis (9, 10). The pAJs, by contrast, are mobile, associate with the radial actin bundles (11, 12), and appear as streaks or puncta, up to several microns in length (10, 13–15). In some AJs, an electron-dense intracellular plaque consisting of cadherin tails and catenins appears uniform along the entire junctional length (10, 14, 16). In many cases, however, such plaques are interrupted by small gaps where density is less prominent and cadherin or catenin signals are sparse (15). A similar organization was detected by Superresolution Structured Illumination Microscopy (SIM) of keratinocyte-like A431 cells that showed that pAJs, ∼1 μm in size, consist of several laterally associated cadherin and nectin clusters interconnected with an actin bundle (17). Importantly, neither light microscopy nor EM studies (18) revealed cadherin clusters on the free cell surface, suggesting that cadherin clustering is induced by cell–cell interactions and is a crucial step in AJ assembly.

This traditional model of AJs was recently challenged by single-molecule localization microscopy (SMLM) of A431D cells (19). This study revealed numerous cadherin clusters with a median size of ∼50 nm that had unexpected properties: they were abundant along the entire cell surface, including cell-contact–free regions, and were not bound to actin filaments. The relationship of these clusters to the traditional view of pAJs remains unclear. Most importantly, their existence strongly contradicts the fundamental concept that trans-cadherin interactions and binding to actin are absolutely essential steps in cadherin clustering and AJ assembly.

Another fundamental, but undefined, aspect of AJ biology is AJ dynamics. Indeed, AJs (pAJs in particular) are mobile, morphologically unstable structures (11, 12), continuously shuffling their adhesive bonds (16). Such plasticity is required so that intercellular contacts can be adjusted as cells reorganize within tissues. Fluorescent Recovery After Photobleaching (FRAP) experiments showed that nearly 100% of cadherin in AJs can be replaced during 1- to 5-min time intervals (11, 20), suggesting that entire AJs can be rebuilt on this timescale. While some

Significance

Adherens junctions (AJs) are major intercellular adhesive structures in vertebrates. Despite the critical role of AJs in tissue integrity and morphogenesis, the detailed organization of their key protein E-cadherin, inside and outside of AJs, remains controversial. Using superresolution microscopy approaches, we show that AJs can reach more than 1 μm in length and consist of tightly packed E-cadherin clusters with crystal-like density interspersed within sparser cadherin regions. No clusters were found outside of AJs. E-cadherin tracking showed that these crystal-like pAJ clusters are transient and their cadherin is reused for new clusters. Our results thus modify the classical view of AJs by depicting them as mosaics of cadherin clusters, whose short lifetimes enable stable overall morphology combined with rapid internal rearrangements.

Author contributions: I.I., J.C., C.-S.C., R.B.T., L.S., B.H., and S.M.T. designed research; I.I., J.C., C.-S.C., R.B.T., and S.M.T. performed research; I.I., J.C., C.-S.C., R.B.T., and S.M.T. contributed new reagents/analytic tools; I.I., J.C., C.-S.C., R.B.T., L.S., B.H., and S.M.T. analyzed data; and I.I., R.B.T., L.S., B.H., and S.M.T. wrote the paper.

Reviewers: B.M.G., Seattle Children's Hospital and University of Washington; and A.Y., University of Queensland.

The authors declare no conflict of interest.

[1]Present address: Department of Biomedical Engineering and Environmental Sciences, National Tsing Hua University, Hsinchu City, Taiwan 300.

[2]To whom correspondence may be addressed. Email: lss8@columbia.edu, bh6@columbia.edu, or s-troyanovsky@northwestern.edu.

This article contains supporting information online at www.pnas.org/lookup/suppl/doi:10.1073/pnas.1720826115/-/DCSupplemental.

Published online April 24, 2018.

evidence suggests that the mechanism driving this phenomenon is cadherin endocytosis (16, 20), no specific flow of cadherin-containing endocytic vesicles from AJs was detected in live imaging experiments (21). Another set of FRAP data, by contrast, showed that up to 50% of cadherin in AJs is immobile during a 5-min period (22–26). It was suggested therefore that AJs consist of a stable adhesive core and a replaceable periphery (23, 26). The processes coordinating the motility and reorganizations of such a stable core between two contacting cells, however, remain puzzling. Clearly, new approaches, other than FRAP, need to be applied to clarify whether AJ homeostasis is based on gradual remodeling of the same clusters or on their complete reassembly. Furthermore, it is important to relate the dynamics of AJs to their structure.

The dual aims of this study are to refine the superresolution description of cadherin distribution in pAJs and, using complementary approaches, to track internal AJ dynamics. In agreement with the traditional view, we show that pAJs of A431 cells appear as micrometer-size adhesion units consisting of dense and loose cadherin regions. Moreover, we find that nonjunctional cadherin is predominantly monomeric. In addition, using two different approaches to label a small fraction of cadherin molecules in pAJs, we show that these structures are continuously and completely reassembled on a subminute timescale. Our structural and live-imaging experiments suggest a dynamic model of AJs, according to which AJ plasticity is based on regulatable actin filament-driven instability of the intrajunctional cadherin adhesive clusters.

Results

AJs Consist of Subregions with Different E-Cadherin Densities. To study the organization of E-cadherin in AJs, we first performed SMLM of A431 cells expressing Dendra2-tagged E-cadherin (A431-EcDn). The basolateral actin/vinculin-associated pAJs of these cells are located very close to and lie nearly parallel to the cell substrate (11, 17). This feature makes these junctions ideal for SMLM. Fig. 1 *A* and *B* show a group of pAJs as detected by wide-field microscopy of Dendra2 fluorescence and by photoactivated localization microscopy (PALM). This approach, in agreement with our previous SIM analyses (17, 21), showed that pAJs consisted of one to three separate submicron-sized clusters (Fig. 1*B*). To approximate their molecular density, the EcDn molecules identified in 30- × 30-nm grids of the correspondingly gridded images were quantified. This analysis showed that the distribution of cadherin-derived signals in pAJs was not uniform and varied from 6 to 12 per grid (Fig. 1 *C*–*F* and *K*, direct count).

We had previously shown that A431-EcDn cells exhibited approximately the same levels of Dendra-tagged and endogenous cadherins (see figure 2C in ref. 11). Assuming the random intermixing of both versions of E-cadherin, the cadherin density in the densest pAJ areas was about 24 molecules per 30×30 nm^2—approximately two times less than that in the cadherin crystal lattice (about 40 molecules per 30×30 nm^2). However, the real cadherin count could significantly deviate from the PALM-obtained numbers since this technique can overcount by counting the same molecule several times or undercount by not detecting some of the molecules (27). It was shown that only

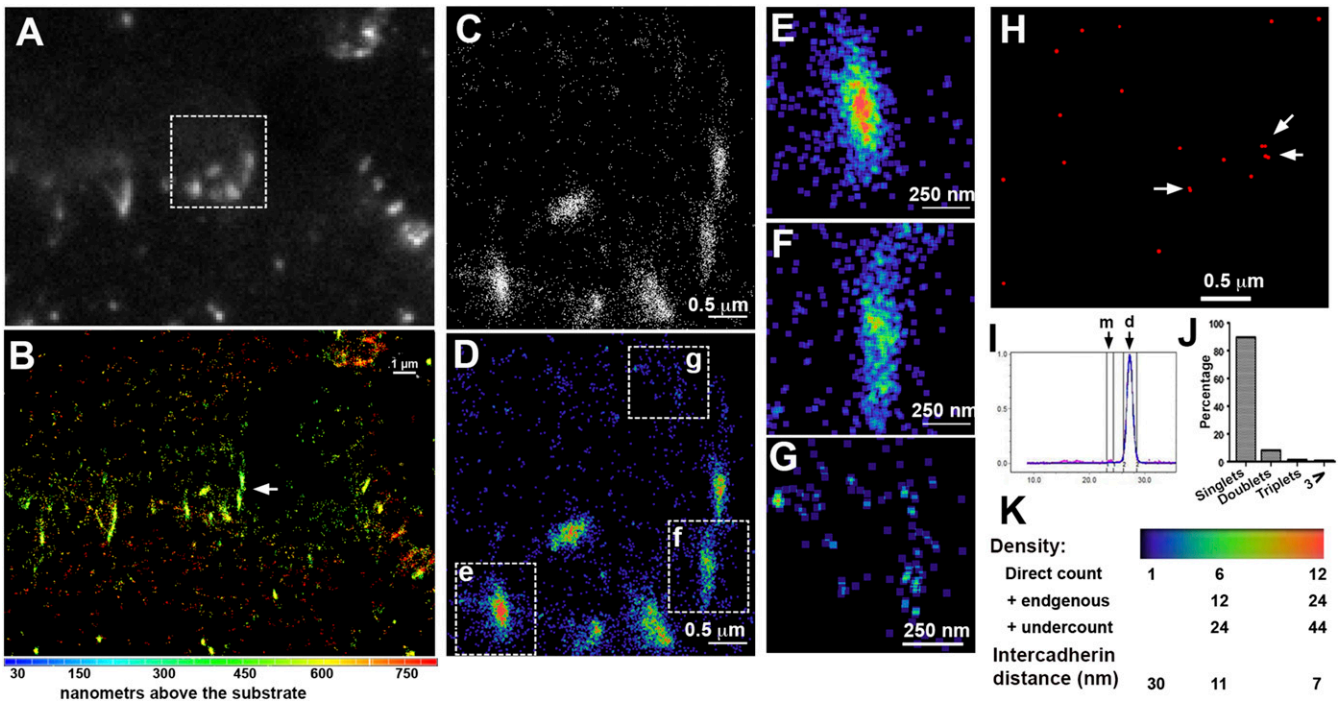

Fig. 1. E-cadherin organization in basolateral AJs of A431 cells. (*A*) Conventional fluorescence microscopy and (*B*) 3D photoactivated localization microscopy (3D-PALM) of the same pAJs of EcDn-expressing A431 cells. Note that most of the pAJs are located at a focus plane, which is about 600 nm above the coverslip. Arrow in *B* points to the pAJ consisting of two microclusters. (Scale bar in *B* also applies to *A*.) (*C*) Enlarged area marked by the dashed box in *A*. Each PALM signal is represented as a white dot. (*D*) The heat map of signal densities in the 30- × 30-nm gridded area shown in *C*. A heat bar showing the signal count in each grid is presented in *K* (direct count). (*E*–*G*) High magnification of the individual pAJs boxed by dashed lines in *D* (marked e, g, and f). Note that pAJs appear as compact structures consisting of regions with different cadherin densities. (*H*) PALM of the recombinant protein, GST-Dn, attached to the coverslip. Each Dn signal appears as a red dot. Arrows show the doublets of signals. (*I*) Size exclusion chromatography of GST-Dn (only a part of the elution profile is shown; m and d stand for monomers and dimers, correspondingly). Note that the protein is a dimer. (*J*) A percentage of GST-Dn signal appearance as detected by PALM. Only 10% of the GST-Dn shows doublets, indicating that PALM recovers less than 50% of molecules. (*K*) A heat bar for the density maps shown in *D*–*G*. Direct count: the counts of PALM-derived EcDn signals per each 30- × 30-nm^2 grid as they appear in *C*; + endogenous, the number of cadherin molecules per grid taking into account the endogenous cadherin; + undercount, the number of cadherin molecules per grid considering the 50% undercounting revealed in *H*–*J*.

10% of Dendra2 molecules are detected more than once (28), but the undetectable fraction of Dendra2 has not been determined.

To assess this fraction, we performed PALM on recombinant GST-Dendra2 (GST-Dn) covalently attached to coverslips. In agreement with the potent dimerization properties of GST (29), this protein formed a stable dimer (Fig. 1*I*). Therefore, if each Dendra2 molecule produces only one PALM signal, GST-Dn should generate doublets of signals. In reality, only 10% of GST-Dn was presented as doublets (Fig. 1 *H* and *J*). This control experiment clearly showed that our SMLM detected 50% or even less of Dendra2 molecules. Such significant undercounting was apparently caused by the low fluorescence intensity of Dendra2, its unspecific bleaching, and/or incomplete Dendra2 maturation. Considering such significant undercounting, our SMLM analysis shows that the pAJs of A431 cells consist of different subregions with a range of cadherin densities. Several, usually central, regions exhibit crystalline lattice-type density (~40/30 × 30 nm^2) while densities of the sparse areas are about two times less (Fig. 1*K*). The number of dense regions per pAJ, while not specifically counted, varies from just a few (pAJ in Fig. 1*F*) to 10 and even more (pAJ in Fig. 1*E*). The size of these regions can reach 100 nm in one of their dimensions.

Extrajunctional Cadherin Is Predominantly Monomeric. We failed to identify the so-called nano-sized cadherin clusters, which were found to be the most prominent form of cadherin organization even on cell–cell contact-free edges of A431D cells (19). Rather, extra-AJ cadherin was predominantly monomeric and only occasionally was detected in small clusters (Fig. 1*G*; see also below).

The majority of the nano-sized clusters in A431D cells were reported to consist of just four to six molecules (19). Therefore, there was a possibility that a dilution of EcDn by endogenous E-cadherin in A431 cells made such clusters undetectable in our study. To test this possibility, we knocked out E-cadherin using CRISPR/Cas9. Several subclones of these A431cEcKO cells expressing EcDn at the level of the endogenous E-cadherin were obtained (Fig. 2*E*). As expected, SMLM of the resulting cells showed a twofold increase in the detectable EcDn density in pAJs (Fig. 2 *A* and *B*). To analyze extrajunctional cadherin clustering in our cells, we determined the clustering index (CI), which we based on the reported median diameter (50–60 nm) of the nano-sized clusters (19). We defined CI as the ratio between the number of 60- × 60-nm^2 regions containing two or more molecules and the number of such regions that contain only a single molecule. The average CI of EcDn in extrajunctional regions was about 0.25 (Fig. 2*C*), suggesting that most of the cadherins in extrajunctional regions are monomeric. Furthermore, a color-coding for the instant of detecting each molecular event showed that the clusters on AJ-free edges were monochromatic. This feature strongly suggests that these clusters are in fact monomeric and originated from Dendra2 molecules, which blinked multiple times before bleaching (28).

Another factor that could render nano-sized clusters undetectable is a low Dendra2 detection rate. To probe this possibility,

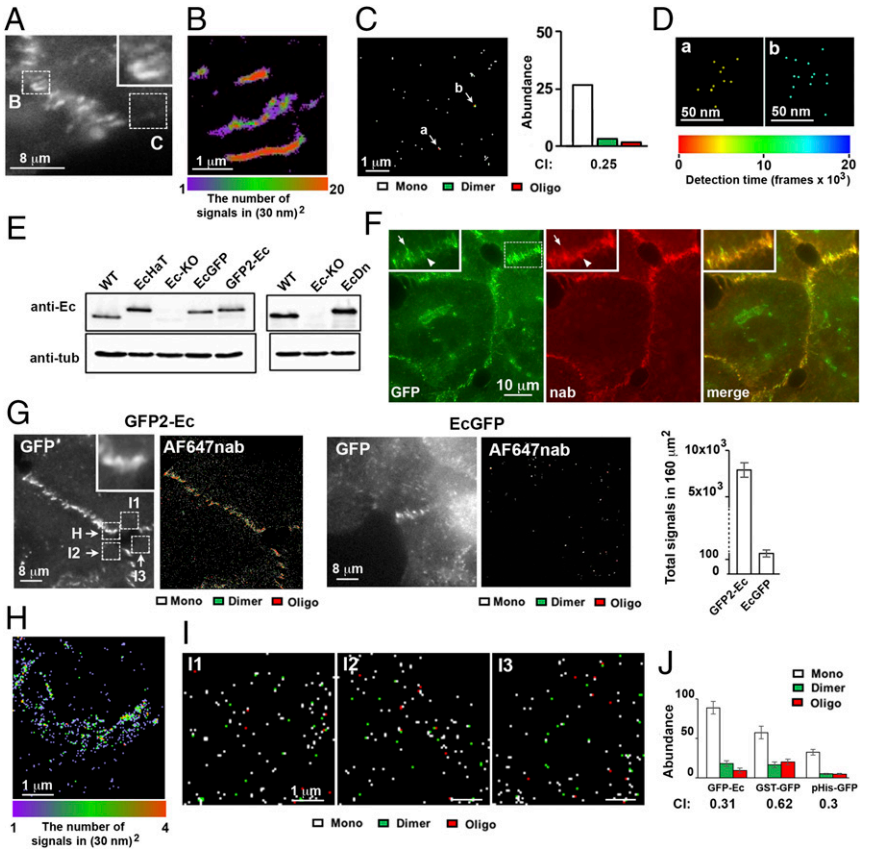

Fig. 2. Extra-AJ organization of E-cadherin. (*A*) Conventional fluorescence microscopy of two cells located at the edge of the colony of EcDn-expressing A431cEcKO cells. A group of pAJs (in the dashed box within *A* labeled "B") is zoomed in the *Inset* (magnification: 2×), and its SMLM image expressing molecular density (direct count of molecules in 30 × 30 nm^2, as in Fig. 1*D*) is shown in *B*. (*C*) Localization of the monomers, dimers, and oligomers (corresponding to numbers of molecules in 60 × 60 nm^2) within the cell–cell contact-free area marked by the box "C" in *A*. Their average abundance within 25-μm^2 areas (six independent areas in two images were quantified) is given at the *Right*. (*D*) Two clusters, "a" and "b" marked in *C*, are zoomed and color-coded relative to the instant of detection. Note that both clusters are monochromatic. (*E*) Western blots of total lysates for cell lines used in this study. (*Left*) WT (parental A431 cells), EcHaT (EcHaT expressed in A431EcKO cells), EcKO (A431EcKO cells), EcGFP, and GFP2-Ec (EcGFP and GFP2-Ec expressed in A431EcKO cells). (*Right*) WT, EcKO, and EcDn (EcDn expressed in A431EcKO cells). (*F*) The A431cEcKO cells expressing GFP2-Ec were stained with AF647nab (2 μg/mL). Note that the nanobody (nab) preferably targets extrajunctional cadherin (arrowhead) but not the pAJs (arrow). (Magnification: *Insets*, 2×.) (*G*) GFP2-Ec–(GFP2-Ec) and control EcGFP- (EcGFP) expressing A431cEcKO cells were stained by AF647nab imaged by conventional microscopy for GFP and by SMLM for AF647 (AF647nab). Monomers, dimers, and oligomers are color-coded (as in *C*). The total number of the AF647nab molecular events is given in the diagram on the *Right*. A group of pAJs (in the dashed box labeled "H") is zoomed in the *Inset* (magnification: 3×). (*H*) The molecular density (number of molecules in 30 × 30 nm^2, as in *B*) of the group of pAJs marked by dashed box "H" in *G*. Note that its apparent density of these pAJs is significantly lower than that based on EcDn (compare with *B*). (*I*) Localization of the monomers, dimers, and oligomers within the cell–cell contact-free areas marked by the dashed boxes *I1*–*I3* in *G*. (*J*) The average abundance of the monomeric, dimeric, and oligomeric signals in contact-free areas (as in *C*) revealed by AF647nab in the GFP2-Ec–expressing cells (GFP-Ec) and on coverslips coated by dimeric (GST-GFP) or monomeric (pHis-GFP) forms of GFP. Their CI is provided below the graph.

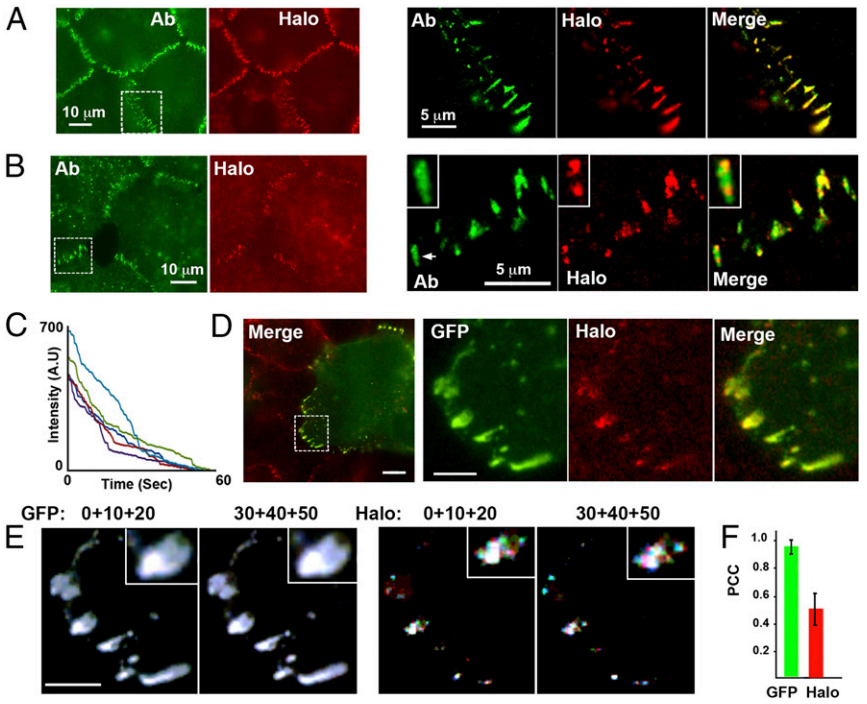

Fig. 3. Dynamics of the intrajunctional HaloTag-tagged clusters. (*A*) The EcadHaT cells were incubated with the 5-μM HaloTag-TMR ligand for 10 min, chased in the ligand-free media for 20 min, and then stained with E-cadherin–specific mAb. The corresponding areas marked by the dashed box are zoomed at the *Right*. Note a nearly complete colocalization of the antibody (Ab)- and HaloTag (Halo)-derived images. (*B*) The cells were incubated with the 0.06-nM TMR ligand for 2 min, chased as in *A*, and stained for E-cadherin. Note the patchy distribution of the labeled molecules in pAJs. The arrow-indicated pAJ is zoomed in the *Inset* (magnification: 2×.). (*C*) Bleaching kinetics of the patchily labeled pAJs. (*D*) The coculture of the EcGFP and Ec-HaT–expressing A431cEcKO cells was labeled as in *C* and time-lapsed at 10-s intervals (Movie S1). The image on the *Left* is a total single frame at time 0. GFP (green) and HaloTag (red) fluorescence is merged. The dashed area of the *Left* image is zoomed in the three *Right* images. The background fluorescence is not subtracted. Note the speckle-like character of the HaloTag fluorescence. (Scale bars, 5 μm.) (*E*) The areas shown in *D* are presented as a sum of three consecutive frames, which are colorized in red, green, and blue, respectively, and merged. Note that the combined GFP-derived images (frames 0 + 10 + 20 and 30 + 40 + 50) are black and white, indicating pAJ stability during 20 s. By contrast, HaloTag-derived images are multicolored. (Scale bar, 5 μm; magnification: *Insets*, 2×.) (*F*) Average PCC of the pAJs between two consecutive frames taken using GFP (GFP) or HaloTag (Halo) fluorescence. The average of 20 pAJs from five independent movies is shown.

we sought an approach to specifically label E-cadherin on the cell surface with a fluorophore that is much brighter than Dendra2. To this end, we expressed in A431cEcKO cells the endogenous level of recombinant E-cadherin in which a mGFP (monomeric GFP) tag was inserted in its ectodomain between Ser306 and Gln307 (GFP2-Ec). *N*-cadherin bearing GFP at this site was shown to be functional (30). Indeed, GFP2-Ec formed AJs that appeared typical for A431 cells (Fig. 2*G*). These cells allowed us to label surface-exposed GFP2-Ec in nonpermeabilized, formaldehyde-fixed cells using an Alexa Fluor 647-conjugated anti-GFP nanobody (AF647nab), which is monovalent, just 4 nm in diameter, and has 1:1 fluorophore/protein molar ratio (31). Wide-field microscopy of the labeled cells showed that the nanobody predominantly labeled the periphery of pAJs but not their brightest regions, as detected by mGFP (arrows in Fig. 2*F*).

SMLM of the labeled cells showed that the molecular density of pAJs was significantly less than in the case of EcDn detection (compare Fig. 2*H* with Fig. 2*B*) since labeling is not expected to be stoichiometric. By contrast, in agreement with wide-field microscopy, the detected cadherin density on the AJ-free edges was much higher (~4 molecules/μm^2, Fig. 2*C*) than in EcDn-expressing cells (~1.4 molecules/μm^2, Fig. 2*I*). This observation showed that AF647nab labeling much more efficiently detected extrajunctional molecules than the Dendra2 tag. The AF647nab staining of these cells was specific since it generated two orders of magnitude more signals than the same labeling of the control EcGFP-expressing cells, in which mGFP is intracellular and hence could not be detected by AF647nab (Fig. 2*G*). Nevertheless, the AF647nab labeling showed that the majority of the open-edge molecules were still monomeric (CI ~ 0.31). To confirm that this CI value was due to monomeric molecules, we determined the CIs of dimeric (recombinant GST-GFP) and monomeric (polyHis-GFP) forms of GFP immobilized on coverslips and stained with AF647nab. Fig. 2*J* shows that the CI of the monomeric GFP (CI ~ 0.3) but not of the GFP dimers (0.62) exactly matches that of the extrajunctional GFP2-Ec. Taken together, these results unequivocally demonstrate that the AJ-free pool of E-cadherin is monomeric in A431 cells.

Cadherin Molecules in AJs Are Rapidly Relocated. While SMLM provides a map of the internal structure of pAJs, its static images do not allow one to determine whether the loose and dense regions are stationary or rapidly reorganized. To probe this question, we sought an approach that allowed us to track a small pool of E-cadherin within each pAJ. To this end, we produced A431-EcKO cells stably expressing recombinant E-cadherin tagged at its C terminus with the Halo tag (EcHaT). The pAJs formed in these cells, which were, as judged by immunofluorescence, indistinguishable in their morphology from those of the WT A431 cells, could be specifically labeled by the HaloTag-TMR (tetramethylrhodamine) ligand (5 μM for 5 min, Fig. 3*A*). To label just a small fraction of cadherin molecules in pAJs, we gradually decreased the ligand concentration. At 0.06 nM, the pAJs exhibited numerous small TMR-labeled speckles, some of which corresponded to the brightest points of pAJs (Fig. 3*B*). Based on bleaching kinetics (Fig. 3*C*), the speckles consisted of a relatively large number of the labeled molecules. Reorganization of such pAJ speckles over time should reflect the internal stability of the entire pAJ structure (32).

To record entire pAJs simultaneously with their TMR-labeled speckles, we cocultured EcHaT cells with A431 cells expressing EcGFP (E-cadherin labeled at the C terminus) and inspected the mixed junctions with GFP- and TMR-labeled sides. Since all molecules on the GFP side are labeled, the green channel reveals the general shape of the junction (Fig. S1). In contrast, the TMR-labeled (red) side of the same pAJ appeared as speckles, the motion of which could be tracked. Time-lapse imaging with 10-s intervals and superimposition of the subsequent frames (Fig. 3 *D* and *E* and Movie S1) demonstrated very fast dynamics of the TMR-labeled speckles. At the same time, the corresponding GFP-labeled side retained its overall appearance. To quantify the internal dynamics of pAJs, we determined the Pearson's correlation coefficient (PCC) of GFP and TMR between the

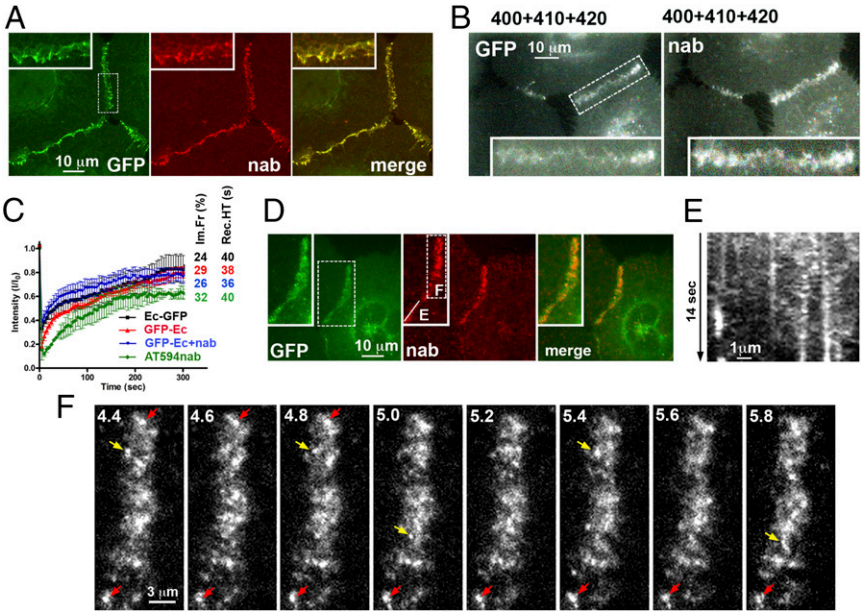

Fig. 4. Fluorescent speckle microscopy of the GFP2-Ecad–expressing cells. (*A*) The cells were incubated with AT594nab (2 μg/mL) for 1 min at 4 °C and then chased for 5 min at 37 °C. Note that AT594nab labeled all AJs. (Magnification: *Insets*, 2×.) (*B*) Time-lapse microscopy acquired in 10-s intervals of the labeled cells. Three consecutive frames of GFP-derived (GFP) and AT594nab-derived (nab) fluorescence were colorized in red, green, and blue (frames taken 400, 410, and 420 s after labeling, respectively) and merged (see Fig. 3*E* for details). The resulting images are black and white for both fluorescences, indicating the overall stability of the labeled pAJs. (Magnification: *Insets*, 2×.) (*C*) Fluorescence recovery curves for cadherin in A431 cells expressing EcGFP- (Ec-GFP, black line), GFP2-Ecad– (GFP-Ec, red line), and GFP2-Ecad–expressing cells labeled with AT594nab as in *A*. In the latter case, FRAP was performed in GFP (GFP-Ec+nab, blue line) and in AT594nab (AT594nab, green line) channels. Mean values of immobile fraction (column "Im.Fr") and recovery half-time (column "Rec.HT") are shown in the corresponding colors. The error bars represent SDs (n = 30). (*D*) The GFP2-Ecad–expressing cells were labeled as in *A*, but at a low AT594nab concentration (0.1 μg/mL). After labeling, the selected region was imaged in the green channel (GFP) and then immediately time-lapsed with five frames per second in the red channel (Movie S2). A single frame (taken 5 s after the start of the movie) is shown (nab). The dashed box in the GFP image is enlarged in the *Insets* (magnification: 1.5×). (*E*) Kymography of the AT594nab fluorescence sampling along the line shown in *D* (nab). (Magnification: 4×, relative to "E" *Inset* in *D*.) (*F*) The ATTO 594 fluorescence in the area demarcated by the dashed box in *D* in eight consecutive frames (time in seconds is indicated). Some of the speckles that persisted in three or more frames are marked by the red arrows. Those that are present only in single frames are shown by yellow arrows.

subsequent frames. This quantification gave a value close to 1 for the GFP-labeled and close to 0.5 for the TMR-labeled junctional sides (Fig. 3*F*). These results clearly show that pAJs, while stable over a time range in seconds, consist of continuously and rapidly reorganizing cadherin molecules.

AJs Consist of Transient Cadherin Clusters. The HaloTag experiments presented above clearly showed that E-cadherin molecules continuously move within pAJs. Unfortunately, the relatively low fluorescence intensity of TMR did not allow us to decrease the pool of the labeled cadherin in pAJs to a size that permits tracking individual molecules. Such labeling, however, is necessary to elucidate the stability of the dense pAJ cadherin regions.

To increase brightness of the labeled molecules, we employed the GFP2-Ecad–expressing cells described in the SMLM section where the GFP is placed within the extracellular domain. Incubation of these cells with ATO 594-conjugated anti-GFP nanobody (AT594nab) at 2 μg/mL for 10 min at 37 °C resulted in complete labeling of all pAJs (Fig. 4*A*). Time-lapse microscopy showed that the labeled pAJs were stationary over a time range of ∼3 min with virtually no detectable internal dynamics either in green (GFP) or in red (ATO 594) fluorescence channels (Fig. 4*B*). A conventional FRAP assay showed that the fluorescence recovery half-time of the nanobody-labeled pAJs was about 40 s, and about 30% of the labeled molecules appeared to be immobile (Fig. 4*C*, blue line). These values are similar to those obtained for the control AT594nab-unlabeled pAJs (Fig. 4*C*, red line) and for the pAJs in EcGFP-expressing cells (black line). These data are consistent with the published FRAP data obtained for C-terminally tagged E-cadherin (22–26) and verified that nanobody labeling did not detectably affect AJ homeostasis.

We then decreased the concentration of nanobody in the labeling media to 0.1 μg/mL. At this concentration, the pAJs exhibited labeled speckles, the distribution of which was very similar to that observed in our HaloTag experiments (compare Figs. 3*D* and 4*D*), indicating that each speckle was formed from the fluorescence of numerous molecules. The exceptional brightness of ATO 594 allowed us to record the labeled speckles with a speed of five frames per second (Fig. 4 *D*–*F* and Movie S2). The obtained movies (Fig. 4*F*) and their kymograph (Fig. 4*E*) showed that the speckles did not change gradually. Instead, their pattern changed by the rapid appearance or disappearance of individual speckles (yellow arrows, Fig. 4*F*). The lifetime of some speckles was just 400 ms, while other persisted for longer than a second (red arrows).

To exclude the possibility that the observed speckles were caused by abnormalities in the behavior of E-cadherin upon AT594nab binding, we produced GFP2-Ecad–expressing, α-catenin–depleted cells. As expected, these cells were unable to form pAJs (Fig. S1, GFP). While their surface E-cadherin was efficiently labeled by AT594nab, no cell–cell contact-located speckles could be detected in these cells (Fig. S2, nab). This observation verified that the dynamic speckles that we observed reflected cadherin dynamics in pAJs. The instant appearance and disappearance of the speckles could be due to the instantaneous (on an approximate second timescale) assembly and disassembly of small, immobile pAJ-located clusters. Alternatively, our data could also be explained by independent relocation of individual cadherin molecules between stationary clusters in pAJs.

To probe these two possibilities, we tracked single cadherin molecules. If cadherin molecules were observed to be immobilized in junctions for periods approximately matching the lifetime of the speckles (on the order of the lifetime of a cluster), this would support the first scenario where clusters assemble and disassemble as a unit. Periods of immobility significantly shorter than the speckles' lifetime would indicate the second possibility where cadherin molecules enter and leave clusters independently. To record single molecules, we decreased the nanobody concentration in the labeling media to 25–50 ng/mL. At this concentration, only individual puncta could be seen in each pAJ. Analyses of the cells fixed after such staining showed that the detectable fluorescent puncta, as expected for single fluorophores, were photobleached in one step (Fig. 5*C*). Low fluorescence of these puncta did not allow us to perform wide statistical analyses of their trajectories. However, all puncta that could be manually tracked showed a consistent motility pattern (Fig. 5 *A* and *B* and Movie S3). The majority of the tracked molecules switched between

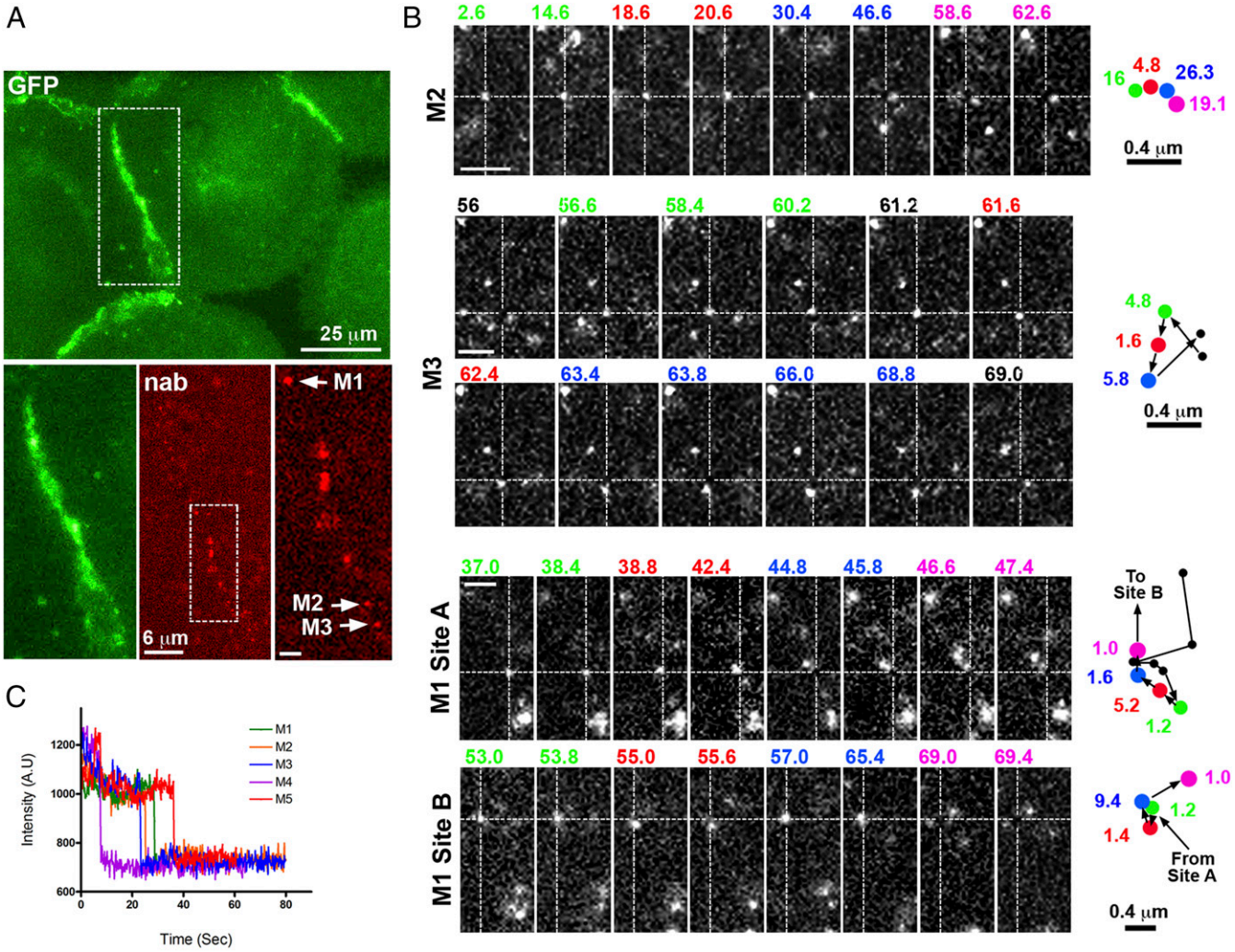

Fig. 5. Single GFP2-Ecad molecule tracking. (*A*) The GFP2-Ecad–expressing A431 cells were labeled as in Fig. 4, but using a very low (50 ng/mL) AT594nab concentration. Before time-lapse recording (five frames per second) of the AT594nab (Movie S3), a single frame of GFP fluorescence (GFP, green) was taken. Its dashed box area is enlarged at the *Bottom* (green). The corresponding AT594nab fluorescence (nab) of the frame taken 60 s after the start of the movie is shown next. The dashed box of this area is further magnified on the *Bottom Right*. (*B*) Three sequences of ATTO 595 fluorescence taken from Movie S3 demonstrating the transient immobility of molecules marked as M1, M2, and M3 in *A*. The first site of immobility of each molecule is placed at the intersection of dashed lines. Only selected frames (numbered according to the time, in seconds, at which they were taken) are demonstrated. The frame times, in which the molecule was immobile at the same site, are color-coded. The maps of the immobile positions (each position has the same color as the color code of the frame number) are shown on the *Right*. The time intervals that the molecules spent at each location are indicated. (Scale bars, 1.5 μm if not specifically indicated.) (*C*) The photobleaching curves of the individual AT594nab puncta. A.U., arbitrary unit.

mobile and immobile modes. In most cases, the consequent stationary positions were spatially very close. Some puncta (Fig. 5*B*, molecule M2) periodically moved just for a pixel-size distance (128 nm). In some cases, however, molecules moved as far as 1 μm between their stationary sites (Fig. 5*B*, molecule M1). Each period of immobility ranged from ∼800 ms to ∼10 s (Fig. 5*B*). Such immobilization periods are consistent with the first scenario, where each cluster behaves as a unit. However, the shortness of the relocation distances, which could be below the microscope resolution and hence undetectable, precluded the exact determinations of cluster lifetime.

Both Sides of AJs Are Relatively Independent. In previous work, we demonstrated that pAJ stability depends on both *cis* and *trans* ectodomain interactions and cadherin anchorage to actin (33, 34). Here we have shown that pAJs consist of independent short-lived clusters. We now ask whether cluster dynamics are driven by active shuffling of cadherin molecules using intracellular machinery or are primarily based on ectodomain interactions. To answer this question, we designed experiments aimed at determining whether cadherin dynamics on both halves of a junction are coupled or independent. We cocultured two populations of A431-EcKO cells; in one, recombinant E-cadherin was tagged with the red fluorescent protein mKate2 (EcKate) and the other with mGFP (EcGFP). In control experiments, we imaged A431 cells coexpressing mGFP-tagged β-catenin (βCatGFP) and EcKate. Time-lapse simultaneous imaging of the red and green fluorescence of the mixed junctions was performed using a two-camera setting.

Visual inspection of the obtained images clearly showed that, while EcKate/βCatGFP fluorescence intensities perfectly matched one another (Fig. 6*A*), the EcKate/EcGFP intensities did not (Fig. 6*C*). To verify this observation, we determined the ratio between red and green fluorescence at each overlapping pixel after background subtraction. This showed that the cadherin/β-catenin ratio was nearly constant in all frames of our movies (Fig. 6*B* and Movie S4). By contrast, pAJs exhibited continuously changing heterogeneity

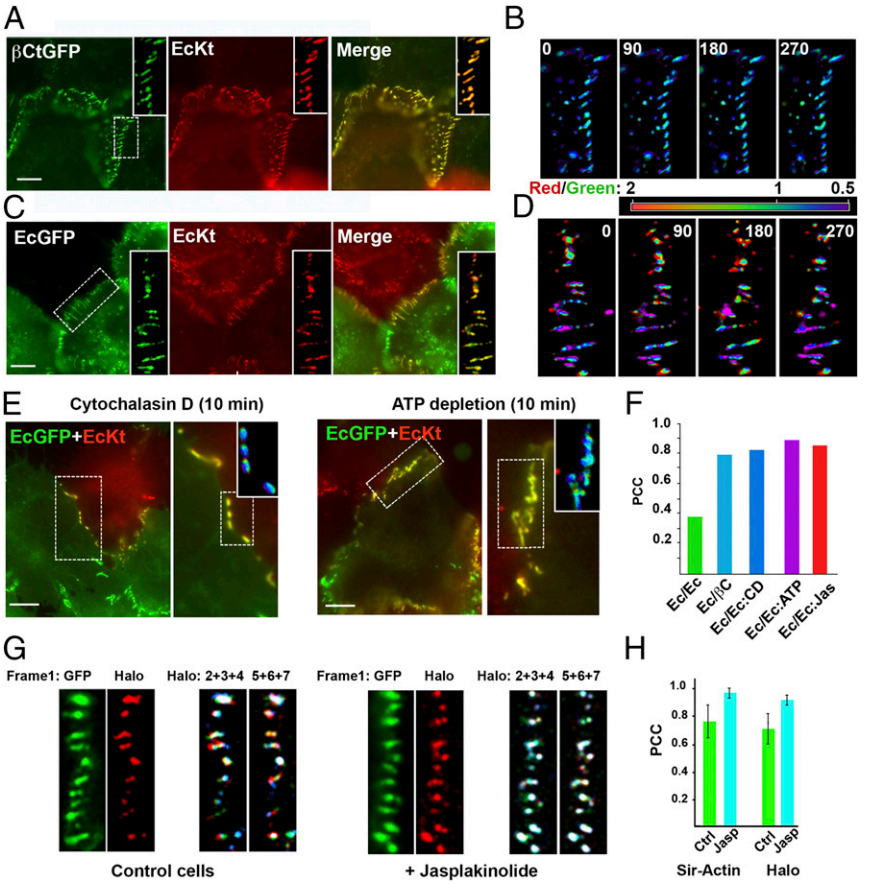

Fig. 6. Differences in cadherin dynamics at two sides of the same AJ. (*A*) The first frame of the movie taken at 90-s intervals of A431 cells coexpressing GFP-tagged β-catenin (βCtGFP, green) and mKate2-tagged E-cadherin (EcKt, red). The boxed area is zoomed in the *Insets* (magnification: 2×). Note the nearly complete identity of green and red fluorescence in the merge image. (*B*) Four consecutive frames of the same movie presented as a ratio of the red to green fluorescence (Movie S4). The color-code bar is at the *Bottom*. (*C*) The first frame of the time-lapse movie (imaged as in *A*) of the coculture of A431 cells expressing either EcGFP (EcGFP) or EcKt (EcKt) E-cadherin. Note that the merge image shows significant variations in green and red intensities of AJs enlarged in the *Inset* (magnification: 2×). (*D*) Four consecutive frames presented as a red-to-green ratio (as in *B*) of the movie shown in *C* (Movie S5). Note significant and changing variations of the ratio. (*E*) Single frames of the movies taken as in *C* but after treatment of the cells with Cytochalasin D or after ATP depletion. The boxed areas are zoomed at the *Right*, and the red-to-green ratios are shown in the *Insets*. (*F*) Average PCC of the pAJs between green and red fluorescence in the cases of cadherin coculture (Ec/Ec), Cytochalasin treatment (Ec/Ec:CD), ATP depletion (Ec/Ec:ATP), or βCatGFP and EcKt coexpression (Ec/βC). (*G*) The coculture of the EcGFP and Ec-HaT–expressing A431cEcKO cells was labeled as in Fig. 3*C* and time-lapsed at 10-s intervals. A single frame shows GFP-derived (GFP, green) and HaloTag-TMR–derived (Halo, red) pAJs within the selected contact between red and green cells. The HaloTag-TMR–labeled pAJs are presented as a sum of three consecutive frames (two sets of frames, numbered, are presented for each movie), which are colorized in red, green, and blue and merged (see Fig. 3*E* for detail). Note that Jasplakinolide notably decreased the differences between frames. (*H*) Average PCC of the pAJs between two consecutive frames taken using HaloTag (Halo) fluorescence in control Jusplakinolide-treated cells. The parallel cultures of EcGFP cells were stained with Sir-actin, and PCC of junctional actin between consecutive frames was determined. The average of 20 pAJs from five independent movies is shown. (Scale bars, 10 μm.) (Magnification in *B*, *D*, and *G*: 1.2×, relative to *Insets* in *A* and *C*.)

in the red-to-green cadherin fluorescence ratio across each AJ (Fig. 6*D* and Movie S5). To quantify the differences in distribution of cadherin on both sides of the same AJs, we performed pixel-by-pixel covariance analyses of red and green fluorescence of pAJs in our movies using PCC. The E-cadherin/β-catenin covariance index was close to 1 in all tested pAJs, while the cadherin/cadherin index was about 0.4.

We then explored the role of the cadherin–actin interactions in the maintenance of the detected asymmetry of the two junctional halves. If actin is a key factor in maintaining junctional asymmetry, one may expect that the changes in the actin cytoskeleton should influence the differences. Indeed, Cytochalasin D (the drug depolymerizing actin filaments) or Jusplakinolide and ATP depletion (both of which inhibit actin filament disassembly) increased PCC of the mixed junctions to ∼1 (Fig. 6 *E* and *F*).

To verify that the actin filament and pAJ dynamics are interrelated, we compared TMR-labeled speckle reorganization in A431 cells expressing HaloTag-tagged E-cadherin (EcHaT, see above) in the presence of Jusplakinolide. While a 10-min-long application of this drug (at 0.1 μM) had no detectable impact on pAJ morphology, it completely stalled actin dynamics as recorded by Sir-Actin staining of living cells (Fig. 6*I*). It also drastically decreased TMR-labeled speckle dynamics (Fig. 6 *G* and *I*). Taken together, these data show that intracellular actin-dependent mechanisms participate in continuous pAJ reorganization.

Discussion

We studied the basolateral pAJs typical for cells of different origin (7, 8, 17, 35). In A431 cells, basolateral pAJs reach 1 μm or longer in length. Our SMLM revealed that each pAJ is not uniform, but exhibits dense and looser cadherin regions. Dense regions are characterized by a crystal lattice-type density (∼3.6 × 10^4/μm^2), suggesting that cadherin here is engaged in *trans*- and *cis*-interactions (33, 36, 37). The looser regions have densities of ∼1–2 × 10^4/μm^2, suggesting that the intermolecular distances here have increased by a factor of ∼1.4–2 relative to the crystalline-like regions. This lower density is not compatible with *cis* interactions, and it is not clear whether *trans* interactions are formed. Notably, the density even in the looser regions is almost four orders of magnitude greater than on the nonadhesive cell edges where it is only approximately four to five molecules per μm^2. These aspects of pAJ structure are shown schematically in Fig. 7. Future studies are needed to clarify several important aspects of this model, one of which is a relationship between cadherin and nectin clusters. According to SIM, these clusters are adjacent to one another (17). A still-unanswered question is whether they are completely separate or, rather, are nectin clusters interspersed within loose cadherin regions.

The mosaic structure proposed here for pAJs is consistent with much of the current literature. Available EM data (10, 13–15) show that dense intracellular plaques in pAJs are broken by gaps where the plaques are not clearly defined and the opposing membranes are disengaged (10, 13, 14). These gaps, therefore, could correspond to the loose cadherin areas in our SMLM images. Notably, this mosaic model of pAJ structure also agrees with our structural understanding of ectodomain assembly through *cis* and *trans* interactions, in that each crystalline-like cluster has a distinct directionality, which prevents its merging

into a single large cluster (33). In this light, regions of lower cadherin density are expected between individual crystalline-like clusters, as is indeed observed in computer simulations of junction assembly (38), and is consistent with recent immune-EM investigations of interaction between cells and cadherin-coated substrates (37).

While our data agree with a large body of EM and cadherin structural data, they are difficult to reconcile with the recent SMLM data published by Wu et al. (19). In contrast to our finding that cadherin clusters are packed within discernible micrometer-size pAJs, Wu et al. reported a large number of tiny, ~50-nm cadherin clusters abundant all over the cells, even on their noncontacting surfaces, regions where we were able to find only cadherin monomers. In part, this inconsistency could be due to the fact that Wu et al. used A431D cells. In our experience, A431D cells, once transfected, contain a high population of cells expressing abnormally high levels of cadherin. Such cells exhibit fluorescence over the entire cell surface. It is possible, for example, that the "nonadhesive" clusters observed by Wu et al. represent cadherin trapped in contacts between plasma membrane protrusions of the same cell.

Another published SMLM study investigated AJs in polarized *Drosophila* epithelia (39). Consistent with our results, this study showed that dense cadherin clusters, some of which are more than 0.5 μm in size, were found exclusively in AJs. The major difference from our work was that the isolated clusters were not joined by the less dense cadherin regions. Their absence could be due to the completely different ectodomain structures of *Drosophila* and human cadherins and also, possibly, to differences in cell types.

While published EM studies together with our cadherin density assessment describe a well-defined anatomy of pAJs, they show only a static view of dynamic structure. Indeed, FRAP and biochemical assays have demonstrated continuous ATP-dependent turnover of cadherin molecules in AJs (11, 20, 24, 25). Both of these techniques, however, were unable to answer a key question: whether this turnover is caused by complete rebuilding of an entire AJ or by partial replacement of some of its structural elements. To shed light on this issue, we labeled a small fraction of cadherin molecules and then tracked these molecules in pAJs. Two complementary labeling approaches, each of which has specific advantages, were used in these experiments.

The first approach involved HaloTag-tagged E-cadherin labeling by a HaloTag TMR ligand. The advantage of this technique is that it directly labels cadherin in AJs. At low concentration of the ligand, this labeling reveals bright intrajunctional speckles composed of numerous labeled cadherin molecules, whose reorganization occurs on a timescale of seconds. Over this time, the overall morphology of pAJs themselves appeared unchanged. These results suggest a significant motion of cadherin within seemingly stable and stationary pAJs. However, due to the relatively high density of the labeled speckles, this approach was not able to determine whether pAJs also contain immobile elements.

The second approach was the labeling of E-cadherin externally tagged with GFP using a red fluorescent anti-GFP nanobody (AT594nab). In agreement with published experiments (30), we found that cells expressing E-cadherin with the GFP tag positioned between Ser306 and Gln307 did not exhibit detectable changes either in AJ morphology or in cadherin dynamics as judged by FRAP assay. Staining of living cells with a low concentration of AT594nab generated transient fluorescent speckles within preexisting pAJs. The advantage of this technique was the exceptional brightness of the resulting speckles, which allowed us to track them on the subsecond timescale. The lifetime of these speckles varied from several hundred milliseconds to several seconds. Importantly, the appearance and disappearance of individual speckles was not gradual but instant. If we assume that AT594nab labeling is random, such instant changes of the labeled speckles indicate the absence in pAJs of any elements that are immobile longer than several seconds. This finding was further validated by tracking AT594nab-labeled single molecules, which exhibited a short-range movement within pAJs from one stationary point to another. While more work is needed to fully describe the behavior of single E-cadherin molecules in pAJs, our results are important since they reveal that cadherin molecules exhibit temporary arrests within micrometer-size adhesions.

Taken together, our recording of cadherin motility showed that pAJs, despite morphological stability over a period of minutes, undergo rapid, within seconds, internal reorganizations. Importantly, none of our approaches detected immobile speckles or single molecules, suggesting that these internal reorganizations involve both the dense and loose E-cadherin pAJ regions. These results show a much more dynamic model of AJs than the one proposed on the basis of FRAP experiments (23, 26). The previous models proposed a gradual recruitment of new molecules around the immobile pAJ core. Such models were based on the fact that the majority of FRAP experiments detected the relatively large (up to 50%) immobile fraction of cadherin molecules in pAJs (22–26). However, in these FRAP experiments, entire junctions were illuminated; clearly, the small, submicron relocations of molecules within the same pAJ—the major pattern of cadherin motion detected by our approaches—would not be detectable by FRAP. According to our dynamic model of pAJs, the cadherin-dense region that we detected within these structures includes several independent adhesive clusters. While determining the exact size and lifetime of the individual clusters will require additional work, our data suggest that the clusters are transient and that cadherin molecules released upon their disassembly are immediately recruited into new clusters. This dynamical depiction of pAJs is compatible with their overall stability, while the continuous rebuilding of pAJs would allow cells to move within tissues without affecting tissue integrity. This proposed mechanism of plasticity might well be common for different structures involved in adhesion. For example, recent data suggest that the continuous turnover of focal adhesions is driven by an analogous assembly/disassembly of small integrin clusters (40, 41).

What might be the driving force for the continuous reassembly of cadherin clusters in pAJs? It seems clear that pAJ assembly is initiated by *trans* recognition between cadherins from apposed cells, followed by the formation of dense clusters mediated by *cis* and *trans* interactions (33, 36, 42, 43). These clusters, in turn, are stabilized by α-catenin, which provides a bridge to the actin cytoskeleton (34, 37, 44, 45). Our data suggest that once this interaction is formed, the cytoskeleton becomes the primary

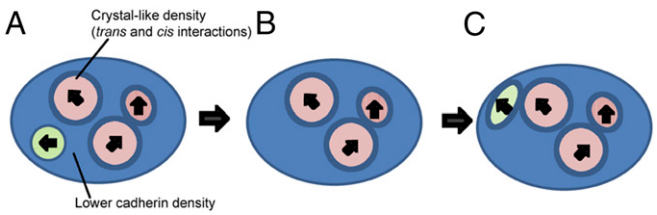

Fig. 7. Mosaic model of pAJ structure and dynamics. An individual pAJ is shown in blue. The pAJ shown consists of four regions of crystal-like density, suggesting that cadherins in these regions are engaged in both *cis* and *trans* interactions, forming an ordered lattice as seen in classical cadherin crystal structures. Each of these subregions has a directionality, indicated by the arrow, which corresponds to the directionality of the cadherin lattice. Between crystalline regions cadherin has lower densities (blue) where its organization is not clear. (*A*) One crystalline cluster is shown in green. (*B*) Such clusters are stable only transiently and disassemble, driven by actin dynamics, as shown by disappearance of the green cluster. (*C*) New clusters reassemble.

determinant of AJ dynamics. This model is supported by our observations that the local cadherin densities and their changes are not strongly correlated in apposed cells and that defects in the actin cytoskeleton induced by Jusplakinolide or Cytochalasin D decrease pAJ asymmetry. It is important to note that this observation along with published data revealing a latrunculin-resistant pool of actin in AJs (2, 6, 22, 46) support tight association of cadherin clusters with actin filaments that is drug-resistant. Thus, actin filaments apparently preserve pAJ integrity in the presence of the inhibitors. In our model (Fig. 7), depolymerization of cluster-associated actin filaments destabilizes the cluster, the cadherin molecules of which are subsequently reused in new clusters, initiated by new actin filament polymerization. The observed cooperativity of α-catenin binding to actin (47–49) may potentially be a key factor in such cadherin reclustering. Notably, these processes take place continuously within a single pAJ, such that its overall morphology appears constant.

In summary, our findings suggest that pAJs comprise mosaics of cadherin clusters with crystal-like density interspersed within high-density, but sparser, cadherin regions. While these junctions display overall morphological stability over minutes, fast dynamic processes occur, which continuously remodel individual junctions.

Materials and Methods

Plasmids. The plasmid (in pRcCMV; Invitrogen) encoding chimeric protein GFP2-Ecad was constructed based on the Kim et al. (30) blueprint. The restriction sites BsiWI and NheI were introduced into the human E-cadherin cDNA between codons Ser306 and Gln307 in the plasmid pRcCMV-Ecad (containing unmodified human Ecad cDNA). These sites were then used for the insertion of the mGFP cDNA (obtained from Addgene, no. 21948). The plasmid encoding mGFP-, mKate2-, and HaloTag at the E-cadherin C terminus was constructed from pRc-EcDn (11) by replacing the tag. All plasmid inserts were verified by sequencing.

Cell Culture, Transfection, and Cell Labeling. Transfection and growth of A431 cells were done as described (11). After transfection and antibiotic selection, the cells were sorted for moderate transgene expression by FACS. The levels of the recombinant proteins exposed on the cell surface were then analyzed by the Western blotting of the surface-biotinylation proteins performed as described earlier (16). To knock out Ecad expression, A431 cells were stably transfected with the plasmid encoding Flag-tagged SP-Cas9 (# 62988; Addgene), and then the clone of these cells (A431cas) was selected using anti-flag staining for the weakest and homogeneous expression of Cas9. Genome editing of these cells was performed using Alt-R CRISPR-Cas9 System (IDT). In brief, the cells were transfected with an RNA complex consisting of Ecad-specific CRISPR RNA (cgccgagagctacacgttca, designed by software of Broad Institute of Harvard and Massachusetts Institute of Technology) and tracrRNA. The Ecad-deficient cell clones were then selected through cloning and verified by Western blotting.

For live-cell imaging the cells were labeled by adding into the cultures for 1–2 min the ATTO 594-conjugated anti-GFP nanobody (Chromotek) at the concentration indicated in the figure legends. After brief washing, the labeled cells were imaged in the label-free imaging media. The HaloTag-tagged AJs were labeled by 0.06 nM HaloTag-TRL ligand (that was 8×10^4 times less than the concentration suggested by the manufacturer protocol) in culture media for 1–2 min, and then the cells were washed several times and incubated in label-free imaging media at least 15 min before imaging.

Immunofluorescence Microscopy. For immunofluorescence, cells were fixed and permeabilized with either methanol–acetone or, in the case of phalloidin staining, with 3% formaldehyde–1% Triton X-100 (17). Wide-field images were taken using an Eclipse 80i Nikon microscope (Plan Apo 100×/1.40 objective lens) and a digital camera (CoolSNAP EZ; Photometrics). The images were then processed using Nikon's NIS-Elements software. The following antibodies were used: mouse anti–E-cadherin, clone HECD1 (Zymed Laboratories); rabbit anti-Dendra2 (Evrogen); goat anti–α-catenin (Santa Cruz Inc.); Alexa Fluor 555-conjugated phalloidin and SIR-Actin were purchased from Invitrogen and Cytoskeleton Inc., respectively.

Live-Cell Imaging and Data Processing. The experiments were performed essentially as described earlier (11, 34) using halogen (Fig. 4), mercury (Fig. 5), or LED (Figs. 3 and 6) light sources. In brief, cells were imaged (in L-15 media with 10% FBS) by an Eclipse Ti-E microscope (Nikon) at 37 °C controlled with Nikon's NIS-Elements software. The microscope was equipped with an incubator chamber, a CoolSNAP HQ2 camera (Photometrics), and a Plan Apo VC 100×/1.40 lens. The 2 × 2 binning mode was used in most imaging experiments. At this microscope setting the pixel size was 128 nm.

Time-lapse images were taken in both FITC and mCherry filter sets (Figs. 4, 5, and 7*A* and ref. 9). For fluorescent speckle microscopy (Fig. 4) and single-molecule tracking (Fig. 5), only the mCherry filter set was used. The FITC filters were used only for taking a single image just before the movies. Two-camera imaging (Fig. 6) was performed using a TwinCam adapter (Cairn Redarch) and two SCimos prime 95B cameras (Photometrix). The cameras' alignment was achieved by addition of fluorescence beads into the imaging chambers.

All images were saved as Tiff files and processed using NIS-Element 4.0.0 (Nikon) or ImageJ software (National Institutes of Health). For kymograph analysis, 15-pixel-deep strips taken from consecutive frames of time-lapse movies were stacked together. For the FRAP assay (Fig. 4*C*), a part of junctions ∼2.5 μm in length was photobleached by an exposure to the 405-nm wave-length laser. Time-lapse images were then taken in red or green channels at 5-s intervals with 1 s of image acquisition time. To display intensity ratio (Fig. 6) or for PCC quantification, the images were processed using NIS-Element 4.0.0 software using limited background reduction, denoising, and then ratio-view or PCC functions.

In single-molecule tracking experiments, three movies, in which particle concentration allowed their accurate tracking, were selected for detailed analysis. The spatial and temporal positions of each molecule were analyzed using Imaris 7.3 (Bitplane) and ImageJ. Background subtraction and fluorescent particle identification were performed using Imaris built-in algorithms with manual compensation. In total, over 300 particles representing single molecules were tracked. Then the accuracy of tracks for 10 molecules from each movie was manually verified and corrected. It showed a high level of errors in the Imaris-based single-molecule tracking that precluded large statistical analyses. The molecule was considered immobile when its fluorescence was confined to the same 3 × 3 pixel (384 × 384 nm) square at least in three subsequent frames. If a molecule became confined to a new 3- × 3-pixel square, which was overlapped with the previous one, it was considered as relocation. Therefore, the shortest distance between the two stationary points was equal to a pixel size of 120 nm.

For the particle photobleaching experiment (Fig. 4*C*), after nanobody staining, the cells were fixed with 3% paraformaldehyde, and time-series images were acquired at a 5-Hz frame rate using a Nikon-Ti inverted microscope equipped with a Plan-Apochromatic total internal reflection fluorescence (TIRF) 100× 1.49 objective lens and iXon3 camera (Andor Technology) at 60% of 561-nm laser intensity.

Single-Molecule Localization Microscopy. For SMLM, the cells were cultured on a glass-bottom dish (P35G-1.5; MatTek) and fixed with 3% paraformaldehyde and 0.1% glutaraldehyde for 10 min at room temperature. After washing three times, the cells were immersed in the freshly prepared image buffer containing 50 mM Tris·HCl (pH 8.0), 10 mM NaCl, 10% glucose, 5 mg/mL glucose oxidase, 0.4 μg/mL catalase, and 0.14 M β-mercaptoethanol. Samples were sealed immediately after adding image buffer. A Nikon *N*-STORM system with a DU897 camera (Andor Technology) was used for superresolution image acquisition. Images (20,000–40,000) were acquired at 29 ms/frame of exposure time via TIRF illumination, using a Plan-Apochromatic TIRF 100× 1.49 objective lens. Dendra-fused proteins were activated with a 405-nm laser and acquired with 561-nm laser illumination. The images were rendered using the built-in *N*-STORM single-molecule localization analysis algorithms.

The recombinant GST and GST-tagged Dendra2 (GST-Dn) were isolated from *Escherichia coli* as described (48). The dimerization status of GST-Dn was verified using the size exclusion chromatography (Agilent 1260 series HPLC, coupled to Superdex-200 column) in conjunction with multiangle light scattering (DAWN HELEOS II; Wyatt Technology). The HPLC column was equilibrated with the buffer containing 5 mM Tris (pH 7.5), 0.2 mM $CaCl_2$, 2 mM $MgCl_2$, and 50 mM KCl.

To covalently attach the recombinant proteins to coverslips, the coverslips were first treated with 4% water solution of 3-aminopropyl-triethoxysilane (Sigma) for 30 min. After rinsing with deionized water, the coverslips were air-dried for 1 h and then incubated with 0.1 μg/mL of GST-Dn (or GST for negative control) for 1 min in PBS. After brief washing with PBS, the GST-Dn remaining on the coverslips was covalently attached to the aminosilane coat by incubating the coverslips in 3% paraformaldehyde and 0.1% glutaraldehyde

in PBS for 5 min at room temperature. Before *N*-STORM imaging the coverslips were treated with 0.1% $NaBH_4$.

ACKNOWLEDGMENTS. We thank Dr. B. Mitchell for valuable discussions and suggestions. Sequencing, flow cytometry, SMLM, and multiangle light scattering were performed at the Northwestern University Genetic, Flow Cytometry, Advanced Microscopy Centers and the Keck Biophysical Facility. The work was supported by National Institutes of Health Grants AR44016 and AR057992 (to S.M.T.) and GM062270 (to L.S.) and by National Science Foundation Grant MCB-1412472 (to B.H.).

1. Harris TJ, Tepass U (2010) Adherens junctions: From molecules to morphogenesis. *Nat Rev Mol Cell Biol* 11:502–514.
2. Green KJ, Getsios S, Troyanovsky S, Godsel LM (2010) Intercellular junction assembly, dynamics, and homeostasis. *Cold Spring Harb Perspect Biol* 2:a000125.
3. Gumbiner BM (2005) Regulation of cadherin-mediated adhesion in morphogenesis. *Nat Rev Mol Cell Biol* 6:622–634.
4. Kobielak A, Fuchs E (2004) Alpha-catenin: At the junction of intercellular adhesion and actin dynamics. *Nat Rev Mol Cell Biol* 5:614–625.
5. Niessen CM, Leckband D, Yap AS (2011) Tissue organization by cadherin adhesion molecules: Dynamic molecular and cellular mechanisms of morphogenetic regulation. *Physiol Rev* 91:691–731.
6. Brieher WM, Yap AS (2013) Cadherin junctions and their cytoskeleton(s). *Curr Opin Cell Biol* 25:39–46.
7. Franke WW (2009) Discovering the molecular components of intercellular junctions: A historical view. *Cold Spring Harb Perspect Biol* 1:a003061.
8. Takeichi M (2014) Dynamic contacts: Rearranging adherens junctions to drive epithelial remodelling. *Nat Rev Mol Cell Biol* 15:397–410.
9. Miyaguchi K (2000) Ultrastructure of the zonula adherens revealed by rapid-freeze deep-etching. *J Struct Biol* 132:169–178.
10. Yonemura S, Itoh M, Nagafuchi A, Tsukita S (1995) Cell-to-cell adherens junction formation and actin filament organization: Similarities and differences between non-polarized fibroblasts and polarized epithelial cells. *J Cell Sci* 108:127–142.
11. Hong S, Troyanovsky RB, Troyanovsky SM (2010) Spontaneous assembly and active disassembly balance adherens junction homeostasis. *Proc Natl Acad Sci USA* 107: 3528–3533.
12. Kametani Y, Takeichi M (2007) Basal-to-apical cadherin flow at cell junctions. *Nat Cell Biol* 9:92–98.
13. Franke WW, Rickelt S, Barth M, Pieperhoff S (2009) The junctions that don't fit the scheme: Special symmetrical cell-cell junctions of their own kind. *Cell Tissue Res* 338: 1–17.
14. Rickelt S, Winter-Simanowski S, Noffz E, Kuhn C, Franke WW (2009) Upregulation of plakophilin-2 and its acquisition to adherens junctions identifies a novel molecular ensemble of cell-cell-attachment characteristic for transformed mesenchymal cells. *Int J Cancer* 125:2036–2048.
15. Wuchter P, et al. (2007) Processus and recessus adhaerentes: Giant adherens cell junction systems connect and attract human mesenchymal stem cells. *Cell Tissue Res* 328:499–514.
16. Troyanovsky RB, Sokolov EP, Troyanovsky SM (2006) Endocytosis of cadherin from intracellular junctions is the driving force for cadherin adhesive dimer disassembly. *Mol Biol Cell* 17:3484–3493.
17. Indra I, Hong S, Troyanovsky R, Kormos B, Troyanovsky S (2013) The adherens junction: A mosaic of cadherin and nectin clusters bundled by actin filaments. *J Invest Dermatol* 133:2546–2554.
18. Kartenbeck J, Haselmann U, Gassler N (2005) Synthesis of junctional proteins in metastasizing colon cancer cells. *Eur J Cell Biol* 84:417–430.
19. Wu Y, Kanchanawong P, Zaidel-Bar R (2015) Actin-delimited adhesion-independent clustering of E-cadherin forms the nanoscale building blocks of adherens junctions. *Dev Cell* 32:139–154.
20. de Beco S, Gueudry C, Amblard F, Coscoy S (2009) Endocytosis is required for E-cadherin redistribution at mature adherens junctions. *Proc Natl Acad Sci USA* 106: 7010–7015.
21. Indra I, Troyanovsky R, Troyanovsky SM (2014) Afadin controls cadherin cluster stability using clathrin-independent mechanism. *Tissue Barriers* 2:e28687.
22. Yamada S, Pokutta S, Drees F, Weis WI, Nelson WJ (2005) Deconstructing the cadherin-catenin-actin complex. *Cell* 123:889–901.
23. Thoumine O, Lambert M, Mège RM, Choquet D (2006) Regulation of N-cadherin dynamics at neuronal contacts by ligand binding and cytoskeletal coupling. *Mol Biol Cell* 17:862–875.
24. Serrels A, et al. (2009) Real-time study of E-cadherin and membrane dynamics in living animals: Implications for disease modeling and drug development. *Cancer Res* 69: 2714–2719.
25. Canel M, Serrels A, Anderson KI, Frame MC, Brunton VG (2010) Use of photoactivation and photobleaching to monitor the dynamic regulation of E-cadherin at the plasma membrane. *Cell Adhes Migr* 4:491–501.
26. Erami Z, Timpson P, Yao W, Zaidel-Bar R, Anderson KI (2015) There are four dynamically and functionally distinct populations of E-cadherin in cell junctions. *Biol Open* 4:1481–1489.
27. Deschout H, Shivanandan A, Annibale P, Scarselli M, Radenovic A (2014) Progress in quantitative single-molecule localization microscopy. *Histochem Cell Biol* 142:5–17.
28. Lee SH, Shin JY, Lee A, Bustamante C (2012) Counting single photoactivatable fluorescent molecules by photoactivated localization microscopy (PALM). *Proc Natl Acad Sci USA* 109:17436–17441.
29. Maru Y, Afar DE, Witte ON, Shibuya M (1996) The dimerization property of glutathione S-transferase partially reactivates Bcr-Abl lacking the oligomerization domain. *J Biol Chem* 271:15353–15357.
30. Kim SA, Tai CY, Mok LP, Mosser EA, Schuman EM (2011) Calcium-dependent dynamics of cadherin interactions at cell-cell junctions. *Proc Natl Acad Sci USA* 108:9857–9862.
31. Kubala MH, Kovtun O, Alexandrov K, Collins BM (2010) Structural and thermodynamic analysis of the GFP:GFP-nanobody complex. *Protein Sci* 19:2389–2401.
32. Danuser G, Waterman-Storer CM (2006) Quantitative fluorescent speckle microscopy of cytoskeleton dynamics. *Annu Rev Biophys Biomol Struct* 35:361–387.
33. Harrison OJ, et al. (2011) The extracellular architecture of adherens junctions revealed by crystal structures of type I cadherins. *Structure* 19:244–256.
34. Hong S, Troyanovsky RB, Troyanovsky SM (2013) Binding to F-actin guides cadherin cluster assembly, stability, and movement. *J Cell Biol* 201:131–143.
35. Huveneers S, et al. (2012) Vinculin associates with endothelial VE-cadherin junctions to control force-dependent remodeling. *J Cell Biol* 196:641–652.
36. Wu Y, et al. (2010) Cooperativity between trans and cis interactions in cadherin-mediated junction formation. *Proc Natl Acad Sci USA* 107:17592–17597.
37. Strale PO, et al. (2015) The formation of ordered nanoclusters controls cadherin anchoring to actin and cell-cell contact fluidity. *J Cell Biol* 210:333–346.
38. Wu Y, Vendome J, Shapiro L, Ben-Shaul A, Honig B (2011) Transforming binding affinities from three dimensions to two with application to cadherin clustering. *Nature* 475:510–513.
39. Truong Quang BA, Mani M, Markova O, Lecuit T, Lenne PF (2013) Principles of E-cadherin supramolecular organization in vivo. *Curr Biol* 23:2197–2207.
40. Shibata AC, et al. (2012) Archipelago architecture of the focal adhesion: Membrane molecules freely enter and exit from the focal adhesion zone. *Cytoskeleton (Hoboken)* 69:380–392.
41. Changede R, Sheetz M (2017) Integrin and cadherin clusters: A robust way to organize adhesions for cell mechanics. *BioEssays* 39:1–12.
42. Hong S, Troyanovsky RB, Troyanovsky SM (2011) Cadherin exits the junction by switching its adhesive bond. *J Cell Biol* 192:1073–1083.
43. Brasch J, Harrison OJ, Honig B, Shapiro L (2012) Thinking outside the cell: How cadherins drive adhesion. *Trends Cell Biol* 22:299–310.
44. Yap AS, Gomez GA, Parton RG (2015) Adherens junctions revisualized: Organizing cadherins as nanoassemblies. *Dev Cell* 35:12–20.
45. Troyanovsky S (2012) Adherens junction assembly. *Subcell Biochem* 60:89–108.
46. Tang VW, Brieher WM (2012) α-actinin-4/FSGS1 is required for Arp2/3-dependent actin assembly at the adherens junction. *J Cell Biol* 196:115–130.
47. Hansen SD, et al. (2013) αE-catenin actin-binding domain alters actin filament conformation and regulates binding of nucleation and disassembly factors. *Mol Biol Cell* 24:3710–3720.
48. Chen CS, et al. (2015) α-Catenin-mediated cadherin clustering couples cadherin and actin dynamics. *J Cell Biol* 210:647–661.
49. Buckley CD, et al. (2014) Cell adhesion. The minimal cadherin-catenin complex binds to actin filaments under force. *Science* 346:1254211.